The Astrophysical Journal Letters, 984:L47 (9pp), 2025 May 10 https://doi.org/10.3847/2041-8213/adccb8

Coincident Multimessenger Bursts from Eccentric Supermassive Binary Black Holes

Vikram Manikantan[1], Vasileios Paschalidis[1,2], and Gabriele Bozzola[1,3]
[1] Steward Observatory & Department of Astronomy, University of Arizona, Tucson, AZ 85721, USA; vik@arizona.edu
[2] Department of Physics, University of Arizona, Tucson, AZ 85721, USA
[3] Division of Geological and Planetary Sciences, California Institute of Technology, Pasadena, 91125 California, USA
Received 2025 January 21; revised 2025 April 11; accepted 2025 April 15; published 2025 May 6

Abstract

Supermassive binary black holes are a key target for the future Laser Interferometer Space Antenna and excellent multimessenger sources across the electromagnetic (EM) spectrum. However, unique features of their EM emission that are needed to distinguish them from single supermassive black holes are still being established. Here, we conduct the first magnetohydrodynamic simulation of disk accretion onto equal-mass, nonspinning, eccentric binary black holes in full general relativity, incorporating synchrotron radiation transport through the dual jet in postprocessing. Focusing on a binary in the strong-field dynamical spacetime regime with eccentricity $e = 0.3$ as a point of principle, we show that the total accretion rate exhibits periodicity on the binary orbital period. We also show, for the first time, that this periodicity is reflected in the jet Poynting luminosity and the optically thin synchrotron emission from the jet base. Furthermore, we find a distinct EM signature for eccentric binaries: they spend more time in a low emission state (at apocenter) and less in a high state (at pericenter). Additionally, we find that the eccentric binary quasiperiodic gravitational-wave (GW) bursts are coincident with the bursts in Poynting luminosity and synchrotron emission. Finally, we discuss how multimessenger EM and GW observations of these systems can help probe plasma physics in their jet.

Unified Astronomy Thesaurus concepts: Black holes (162); Gravitational waves (678); High energy astrophysics (739); Magnetohydrodynamical simulations (1966); General relativity (641); Jets (870); Accretion (14)

1. Introduction

The inspiral and merger of supermassive binary black holes (SMBBHs) are main targets for the future space-based gravitational-wave (GW) Laser Interferometer Space Antenna (LISA; M. Colpi et al. 2019; J. I. Thorpe et al. 2019; P. Amaro-Seoane et al. 2023). At least a fraction of SMBBHs are expected to exist in hot gas (J. E. Barnes 2002; X. Chen et al. 2009; C. Rodriguez et al. 2009; S. Li et al. 2019). This makes them ideal for multimessenger astronomy because, in addition to GWs, gas accretion will drive emission across the electromagnetic (EM) spectrum (see T. Bogdanovic et al. 2022 for a recent review). Pulsar timing arrays also target SMBBHs, but unless their sensitivity increases significantly (P. A. Rosado et al. 2015; L. Z. Kelley et al. 2018; K. Aggarwal et al. 2019; A. Afzal et al. 2023; S. Babak et al. 2024), detecting GWs from individual SMBBHs may have to wait until the mid-2030s for the launch of LISA.

Identifying EM signals that are unique to SMBBHs is essential to maximizing the scientific yield of multimessenger astronomy (J. D. Schnittman 2011; T. Bogdanovic et al. 2022), as coincident observations of EM and GW signals can probe fundamental physics, gravity, astrophysics, and cosmology (J. Baker et al. 2019; M. Colpi et al. 2019; J. I. Thorpe et al. 2019; K. G. Arun et al. 2022; P. Amaro-Seoane et al. 2023). Over 200 SMBBH candidates have been identified through sky surveys (C. Rodriguez et al. 2006, 2009; M. Charisi et al. 2015; M. J. Graham et al. 2015; T. Liu et al. 2019; S. O'Neill et al. 2022; S. Kiehlmann et al. 2024), including more than 25 inferred to be in the strong-field dynamical regime (see Figure 1 in J. C. Bright & V. Paschalidis 2023). To evaluate these potentially relativistic candidates, we must use theoretical models of SMBBH accretion to predict their smoking-gun EM signatures.

To reliably model SMBBHs from first principles during their late inspiral and merger requires simulations in full general relativity (GR) coupled to magnetohydrodynamics (MHD), microphysics, and radiation. Performing such simulations with existing computational resources and numerical methods is not currently feasible due to the vast range of length and timescales involved. So, to make progress at this time, we have to make simplifying assumptions. Some methods forego dynamical relativistic gravity (E. R. Most & H.-Y. Wang 2024, 2025) and use 2D simulations (see, e.g., D. J. Muñoz et al. 2020; J. R. Westernacher-Schneider et al. 2022; D. Lai & D. J. Muñoz 2023; S. DeLaurentiis et al. 2025; and references therein for recent work). Others adopt post-Newtonian background metrics (see, e.g., M. J. Avara et al. 2024; K. Porter et al. 2025; and references therein for recent work). Finally, fully general-relativistic 3 + 1 approaches solve the Einstein equations without approximation (see R. Gold 2019 and F. Cattorini & B. Giacomazzo 2024 for recent reviews). To date, no studies have treated microphysics or full radiation transport in 3 + 1 general-relativistic magnetohydrodynamic (GRMHD) simulations.

Recent studies of accretion onto binary black holes (BBHs) in full 3 + 1 GR have investigated various parameters (R. Gold et al. 2014b; A. Khan et al. 2018; V. Paschalidis et al. 2021; F. Cattorini et al. 2022; J. C. Bright & V. Paschalidis 2023; M. Ruiz et al. 2023; G. Fedrigo et al. 2024). However, accretion onto eccentric SMBBHs in full GR remains unexplored. Treating eccentricity is important, as an increasing number of works show that disk–SMBBH interactions can excite substantial binary orbital eccentricity (A. Franchini et al.

2024; C. Roedig et al. 2011; M. Siwek et al. 2024; R. Valli et al. 2024).

Although GWs tend to circularize orbits as the binary inspirals (P. C. Peters & J. Mathews 1963), nonnegligible eccentricity can remain down to the late inspiral depending on disk and binary parameters. Assuming thin disks, $H/R \sim \mathcal{O}(0.01)$, BBHs with mass $M < 10^6\ M_\odot$, and mass ratio $q \lesssim 0.1$, the eccentricity in the LISA band can potentially be $\mathcal{O}(0.1)$ (C. Roedig et al. 2011). However, the residual eccentricity in the LISA band depends (among other things) on the binary–disk decoupling radius, which shrinks with increasing H/R (B. D. Farris et al. 2012). For thin disks, this radius can be $\mathcal{O}(200M)$, in which case the BBH can radiate away most of its eccentricity before or as it enters the LISA band. For thicker disks ($H/R \sim 0.1$, relevant, e.g., for slim disks, M. A. Abramowicz et al. 1988), the decoupling radius can be as small as $30M$ (B. D. Farris et al. 2012), and the matter torque on the binary can be maintained for longer, allowing the binary to maintain higher eccentricity as it enters the LISA band. Therefore, it remains an open question as to what range of BBH mass and mass ratio binaries in a slim disk environment can achieve high-eccentricity as they enter the LISA band. Additionally, chaotic nonhierarchical three-body interactions—which can arise following a triple galaxy merger (J. Yadav et al. 2021; Y. Ni et al. 2022)—can excite orbital eccentricity up to order unity even at relativistic separations (T. Ryu et al. 2018).

Moreover, eccentric binaries probe more relativistic velocities than quasi-circular ones (at the same orbital period), and even one high-eccentricity binary detection could provide a wealth of opportunities for probing extreme gravity and astrophysics. Therefore, studying theoretically high-eccentricity binaries in the dynamical spacetime regime is very important.

In this work, we present the first $3 + 1$ full GRMHD simulation of circumbinary disk (CBD) accretion onto a BBH with initial eccentricity $e = 0.3$ and perform the first synchrotron radiation transport calculation through the dual jet in postprocessing. While the value of eccentricity we use here may be high by traditional astrophysical expectations for comparable-mass binaries, it provides the basis for our point-of-principle calculations and addresses three key questions: (i) How does orbital eccentricity impact the mass accretion rate and its periodicity?, (ii) How does it affect the Poynting luminosity and synchrotron emission?, and (iii) What is its impact on the multimessenger picture of these sources?

This Letter is structured as follows: in Section 2, we describe the methods we adopt; in Section 3, we describe the accretion flow onto the binary and jet launching; in Section 4, we report the results of our radiative transfer calculation of synchrotron emission within the jet and discuss its potential detectability and the simultaneous GW and EM emission from our models, and in Section 5, we conclude with a discussion of our findings. Unless otherwise stated, we adopt geometrized units in which $G = c = 1$.

2. Methods

2.1. Initial Data

Spacetime. We use the `TwoPunctures` thorn to generate the spacetime initial data for an equal-mass, nonspinning, eccentric BBH (M. Ansorg et al. 2004; V. Paschalidis et al. 2013). The BHs are initialized at apocenter with coordinate separation $d/M \sim 26$. We introduce orbital eccentricity by first computing the third-order post-Newtonian linear momenta corresponding to a quasi-circular BBH and then adjusting their tangential component by a factor of $\sqrt{1-e}$, where e is our target eccentricity. In a follow-up paper, we provide the details on how we measure the binary eccentricity from our simulations, along with comparisons with additional eccentricities and with a quasi-circular binary (V. Manikantan et al. 2025).

Matter. We adopt the power-law torus solution for the matter initial conditions as previously described in R. Gold et al. (2014b) and A. Khan et al. (2018). We set the inner edge of the CBD at $r/M = 18$ with specific angular momentum of $l = 5.15$ and disk outer edge at $r/M \simeq 100$. We use a Γ-law equation of state, with $\Gamma = 4/3$—appropriate for radiation-dominated disks. We seed the disk with a poloidal magnetic field as in A. Khan et al. (2018). The initial magnetic field renders the CBD unstable to the magnetorotational instability (MRI; S. A. Balbus & J. F. Hawley 1991).

2.2. Evolution

Spacetime. We evolve the spacetime by solving the full Einstein equations in the Baumgarte–Shapiro–Shibata–Nakamura (BSSN) formalism (M. Shibata & T. Nakamura 1995; T. W. Baumgarte & S. L. Shapiro 1998) as implemented in the `LeanBSSN` code using sixth-order finite differences (U. Sperhake 2007). We adopt the moving puncture gauge conditions (J. G. Baker et al. 2006; M. Campanelli et al. 2006) with the shift vector parameter η set to $\eta = 1.4/M$.

Matter. We employ the 3D GRMHD, adaptive-mesh-refinement (AMR) `IllinoisGRMHD` code (Z. B. Etienne et al. 2015) within the `Einstein Toolkit` (L. Werneck et al. 2023), which employs the Cactus/Carpet infrastructure (T. Goodale et al. 2003; E. Schnetter et al. 2016). `IllinoisGRMHD` evolves the equations of ideal MHD in flux-conservative form via the Harten, Lax, and van-Leer Riemann solver (E. F. Toro 2009), and the piecewise-parabolic method for reconstruction (P. Colella & P. R. Woodward 1984). These methods have been described in Z. B. Etienne et al. (2015) and have been extensively tested against other codes in O. Porth et al. (2019). For our EM gauge choice for the vector potential formulation of the induction equation, we use the generalized Lorenz gauge condition of Z. B. Etienne et al. (2012) and B. D. Farris et al. (2012) and set the Lorenz gauge damping parameter to $\xi = 8/M$. Finally, the fluid does not backreact onto the spacetime, since the spacetime mass/energy content is dominated by the SMBBH.

Grid. We adopt `Carpet` (E. Schnetter et al. 2016) for AMR. We use a three-dimensional Cartesian grid with the outer boundary extending from $-5120\,M$ to $+5120\,M$ in the x-, y-, and z-directions, with a total of 14 refinement levels. We have three sets of nested AMR boxes, one centered on the center of mass and two centered on each of the two BHs in the binary. The half-side-length of an AMR level i is $5120 \times 2^{-(i-1)}M$, $i = 1, \ldots 14$. The grid spacing on the coarsest (finest) refinement level is $\Delta x = 128\,M$ ($\Delta x = M/64$). We do not treat radiative feedback, heating, or cooling. We resolve the fastest-growing mode MRI wavelength with at least 20 zones in the disk and a maximum of 50 zones at the inner edge of the disk.

Diagnostics. We adopt the same diagnostic tools as in J. C. Bright & V. Paschalidis (2023) to measure the rest-mass

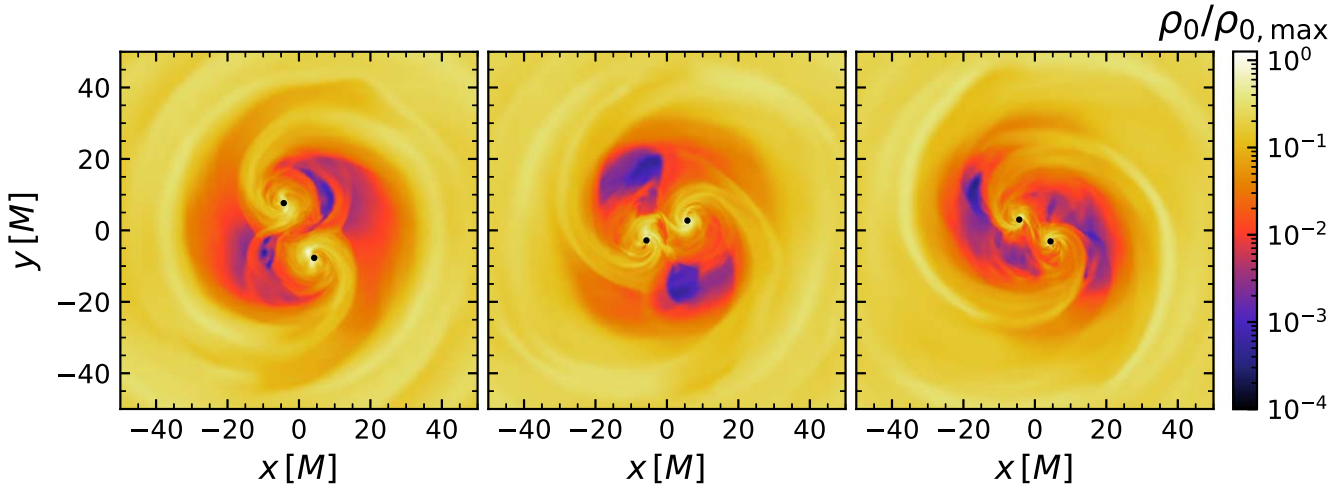

Figure 1. Contours of rest-mass density (ρ_0) normalized to the initial maximum density $\rho_{0,max} = 2.6 \times 10^{-11}(\langle \dot{M} \rangle / 0.1 \dot{M}_{\rm edd})(M/10^7 M_\odot)^{-1}(\eta/0.1)^{-1}\,{\rm g\,cm^{-3}}$, where $\dot{M}$ is the accretion rate and $\dot{M}_{\rm edd}$ is the Eddington accretion rate for a gravitational mass M and radiative efficiency η. The left panel corresponds to the binary just after apocenter ($t/M = 4120$); the center show the binary as it approaches pericenter ($t/M = 4220$); and the right panel shows the binary at pericenter ($t/M = 4300$). We indicate the BH horizons with black disks. In the left panel, tidal streams circularize to form minidisks. In the center panel, these minidisks begin to accrete, and in the right panel, they are depleted at pericenter. Once in a quasi-steady-state, the binary exists in the cavity with density $\rho_0/\rho_{0,max} \sim 10^{-3}$–$10^{-2}$.

accretion rate ($\dot{M}$) and outgoing Poynting flux. The latter we compute on a sphere of coordinate radius $200\,M$ from the binary center of mass, thereby encompassing the entire BBH–disk system.

We locate apparent horizons with `AHFinderDirect` (J. Thornburg 2004). We perform all Fourier analysis with the `scipy.fft` function (P. Virtanen et al. 2020). We measure the orbital frequency of the binary with the fast Fourier transform (FFT) of the first time derivative of the unfolded phase (φ) of the $\ell, m = (2, 2)$ mode, $f_{22} \equiv \frac{d\varphi}{dt}$, which we extract using the `NPScalars` thorn part of the Canuda suite (H. Witek & M. Zilhão 2015; H. Witek et al. 2021). We use the package `kuibit` (G. Bozzola 2021) for all our analyses.

2.3. Synchrotron Modeling

To model synchrotron emission, we solve the radiation transfer equation, Equation (1.23) of G. Rybicki & A. Lightman (1991), using the synchrotron emissivity given by Equation (6.36) of G. Rybicki & A. Lightman (1991) multiplied by $1/4\pi$, i.e., we average out the distribution over the solid angle. Moreover, in the emissivity, we average the pitch angle, α, out of the equation by assuming that the electrons follow an isotropic pitch-angle distribution between $0 < \alpha < \pi/2$. We adopt the synchrotron self-absorption coefficient given by Equation (6.53) of G. Rybicki & A. Lightman (1991). This emissivity and absorption coefficient corresponds to a power-law electron distribution $N(E)\,dE = CE^{-p}\,dE$. This distribution has two constants that define it for a given p: C and the miminum electron energy $E_{\rm min}$. To compute C, we impose charge neutrality with the ion density in our simulations, and we compute $E_{\rm min}$ by adopting a fixed ratio between the electrons and the magnetic field energy density of 10%. We also set $E_{\rm min} = 2m_e c^2$, where m_e is the electron mass, as an alternative. For thermal synchrotron, we follow G. Rybicki & A. Lightman (1991) and A. Tsouros & N. D. Kylafis (2017).

3. Results

3.1. Accretion Flow

We initialize a gaseous torus around the BBH (as detailed in Section 2) and evolve the system until the accretion rate approximately relaxes (after ∼six orbits). In Figure 1, we plot the rest-mass density of the gas on the BBH orbital plane at representative times: at pericenter (left), at apocenter (right), and an intermediate time (middle). We indicate the BH apparent horizons with black disks. The gas density is normalized to the initial maximum gas density in the torus, $\rho_{0,max}$. The BHs continue to reside in a lower-density cavity ($\rho_0/\rho_{0,max} \sim 10^{-3}$) within the higher-density CBD ($\rho_0/\rho_{0,max} \sim 1$). As the binary approaches the CBD inner edge, at its apocenter, it tidally torques the CBD, and matter from the inner disk edge falls onto each BH through high-density tidal streams. The infalling gas temporarily circularizes around each BH, creating a minidisk (left panel in Figure 1), which begins to be depleted as the binary approaches the next pericenter passage (middle and right panels in Figure 1). This process repeats quasiperiodically as the BBH inspirals.

In the left panel of Figure 2, we plot the time-dependent total rest-mass accretion rate onto the BHs (black solid line) and the accretion rate onto the individual black holes (dashed and dotted–dashed lines). Both exhibit quasiperiodic behavior. The mass accretion rate is initially high ($t/M < 4000$) and decreases with time for two reasons: (1) there is a transient phase due to the initial data relaxation, and (2) the binary is inspiraling rapidly due to its higher initial eccentricity. Due to the combination of these two effects, the inner disk relaxes (as measured by the accretion rate) for $t/M > 4000$. In particular, after $4000\,M$, the accretion rate reaches a quasi-steady state, as indicated by its near-constant amplitude and variability versus time.

In the right panel of Figure 2, we plot the Fourier transform of the total rest-mass accretion rate for the time range $3000 < t/M < 5500$, which corresponds to about five binary orbits. The Fourier plot demonstrates that the dominant frequency of accretion rate variability is the orbital frequency, $f \sim f_{\rm orb}$. This periodicity is consistent with recent Newtonian

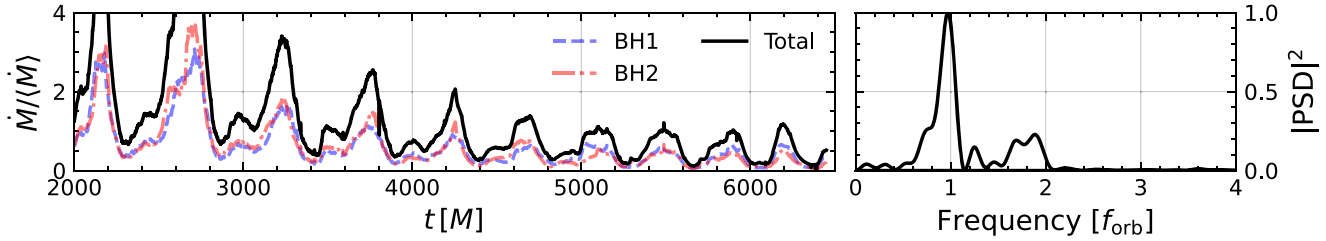

Figure 2. Left: rest-mass accretion rates onto both BHs (solid black line) and onto the individual black holes (dashed and dotted–dashed lines), all normalized by the total average for $3000 < t/M < 5500$. Right: power spectral density (PSD) of the Fourier transform of the total rest-mass accretion rate, with the frequency normalized to the BBH orbital frequency. The Fourier transform is performed on the time period $t = 3000$–$5500\,M$. The dominant frequency for accretion is $f \sim f_{\mathrm{orb}}$ and is insensitive to the time interval over which we perform the Fourier transform.

hydrodynamic studies of eccentric binaries (J. R. Westernacher-Schneider et al. 2022; S. DeLaurentiis et al. 2025), which are valid for substantially larger orbital separations. The measured accretion rate periodicity of f_{orb} in the eccentric case is fundamentally different from the periodicity in quasi-circular binaries, where the accretion rate is modulated at $1.4f_{\mathrm{orb}}$ (V. Paschalidis et al. 2021; J. C. Bright & V. Paschalidis 2023). The reported periodicity from the FFT is robust and remains at $1f_{\mathrm{orb}}$ even if we choose to perform it for $t/M > 4000$. The additional power we see in the power spectral density (PSD) between 1 and $2f_{\mathrm{orb}}$ is likely due to the initial relaxation of the fluid because it disappears if the Fourier transform is performed for $t > 5000\,M$. We defer a detailed discussion of the dynamics and periodicity mechanisms in eccentric BBHs to a follow-up work (V. Manikantan et al. 2025).

3.2. Jet Launching

We observe dual-jet launching along the BBH orbital angular momentum axis consistent with previous CBD studies in full GR with nonspinning black holes (B. D. Farris et al. 2012; R. Gold et al. 2014a, 2014b; A. Khan et al. 2018; V. Paschalidis et al. 2021; J. C. Bright & V. Paschalidis 2023). In Figure 3, we plot the plasma magnetization ($\sigma \equiv b^2/2\rho_0$) of our BBH–CBD system on the x–z-plane to describe the vertical dual-jet structure. The BHs exist on the x–y-plane ($z/M = 0$) and launch jets in the $\hat{z}$-direction, which merge for $|z|/M \gtrsim 20$. These regions are magnetically dominated $\sigma > 1$ and extend out to $|z| > 200\,M$. On either side of the BBH, at $z/M \sim 0$, exists the CBD with low plasma magnetization $\sigma \sim 10^{-4}$. We show the magnetic field structure with directed white lines, which we plot over the plasma magnetization. In the jet regions above and below the BBH, the magnetic field is highly ordered and extends vertically out to $|z| > 200\,M$.

4. Synchrotron Radiative Transfer

To determine possible EM emission from these jet regions, we perform a synchrotron radiative transfer calculation of our simulations in postprocessing. In this section, we outline the key assumptions of our calculations and present spectral energy distributions (SEDs) of the jet synchrotron emission. We include a more detailed presentation of our synchrotron modeling and a derivation of the analytic scaling of the SED with the accretion rate and the BBH mass in a follow-up paper (V. Manikantan et al. 2025).

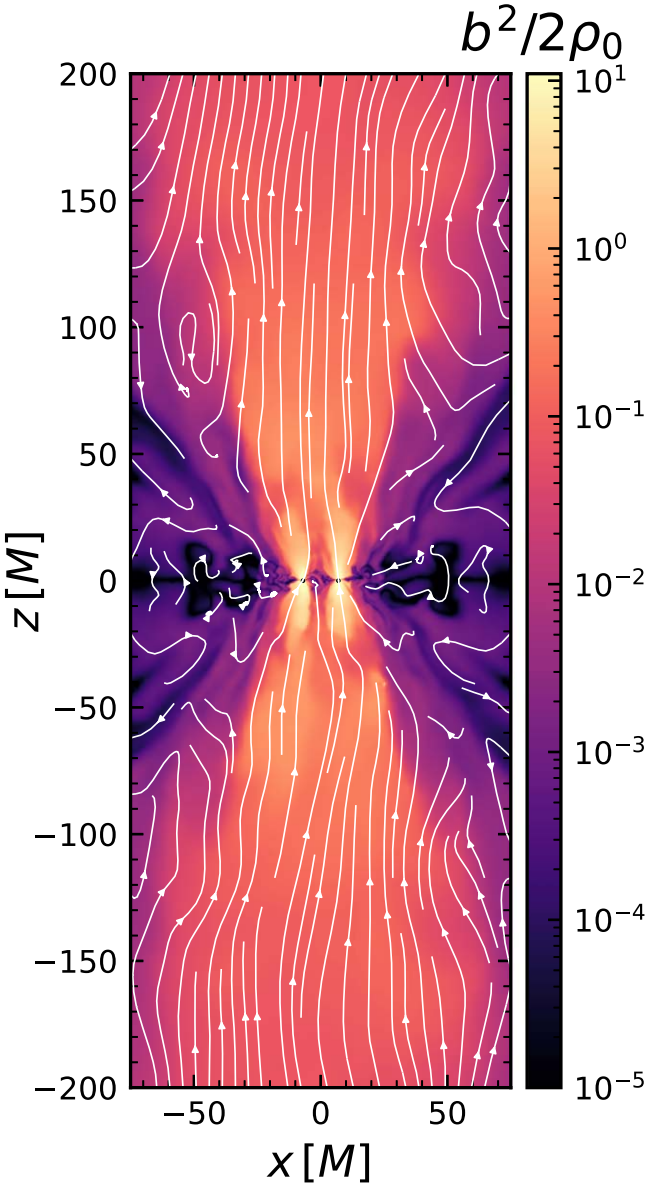

Figure 3. Contours of plasma magnetization ($\sigma \equiv b^2/2\rho_0$) on the x–z-plane at $t/M = 4197.6$. The BHs are at $x/M \pm 10$, $z/M = 0$. Immediately below and above the BHs are regions of high plasma magnetization $\sigma \sim 10^0$–10^1, which extend vertically to $|z| > 200\,M$. To the left and right of the BHs is the CBD, which has lower plasma magnetization $\sigma \sim 10^{-3}$–10^{-5}. The magnetic field (overplotted with directed white lines) is highly ordered above and below the BHs, indicating the jet regions.

4.1. Motivation and Setup

Relativistic electrons within the jet's magnetic field can produce synchrotron emission across the EM spectrum (see, e.g., C. C. Cheung et al. 2007; J. Y. Kim et al. 2018; R. C. Walker et al. 2018; D. J. Saikia 2022). The interaction of the dual jets can give rise to current sheets and kink instabilities, which can then lead to a population of nonthermal electrons with power-law distribution (E. Alves et al. 2018; M. Petropoulou et al. 2019; T. E. Medina-Torrejón et al. 2021; E. M. Gutiérrez et al. 2024). Motivated by this, we make the following approximations in our synchrotron modeling:

1. We adopt a power-law electron distribution, assuming the local electron energy density equals 10% of the local magnetic energy density in the jet (M. A. Scott & A. C. S. Readhead 1977; R. A. Chevalier 1998; A. Panaitescu & P. Kumar 2002; M. Petropoulou et al. 2019). This fraction is motivated by Figure 6 in M. Petropoulou et al. (2019) where the electron energy is ∼10% of the magnetic energy density; in reality, there is no widely accepted fraction to use here, but our reported periodicities of the synchrotron spectrum are independent of this fraction. We also tested a power-law distribution with minimum electron energy corresponding to a Lorentz factor of 2, as well as electrons with a thermal distribution (G. Rybicki & A. Lightman 1991; A. Tsouros & N. D. Kylafis 2017).
2. We start our integrations at a height of $z/M = 50$ above the orbital plane. This is because we do not perform a general-relativistic radiative transfer calculation; therefore, our integration of the radiative transfer equation must be in approximately flat spacetime. However, we confirmed that the shape of the synchrotron spectrum and its variability are robust for integrations starting at $z/M = 20$ and $z/M = 30$.
3. We adopt the "fast light" approximation; we solve the radiative transfer equation on a slice of constant coordinate time. This approximation is valid when the medium does not change much on a light-crossing time, which in our case is valid for the optically thin synchrotron frequencies.
4. We do not treat special relativistic effects other than those going into the computation of the synchrotron emissivity and absorption coefficients. This assumption is consistent with the fact that the plasma in the jet base in our simulations is only mildly relativistic ($v/c \sim 0.3$).

In this work, we choose the power in the electron power-law distribution to be $p = 2.5$; in our follow-up extended paper, we demonstrate that our reported results on the shape and the variability of the synchrotron spectrum are insensitive to p, and we report the synchrotron spectra for a quasi-circular and another eccentric binary (V. Manikantan et al. 2025). Lastly, we only report results from a viewing angle of $\theta = 0$; in other words, we treat the system as a blazar. We solved the radiative transfer equation for other viewing angles and found that the shape and variability of the synchrotron spectrum are insensitive to the viewing angle for a given integration starting height. For the time dependence of the synchrotron spectrum, we solve the radiative transfer equation with a cadence of $\sim 3.6\, GM/c^3$ and produce SEDs for each slice of constant coordinate time.

4.2. Synchrotron Emission

In the left panel of Figure 4, we plot the SED vs time, assuming a $10^7\, M_\odot$ BBH accreting at 10% Eddington, which is appropriate for our simulation of a thick accretion disk without full radiation transport. Given that we find very weak angular dependence of the specific intensity, to compute the specific luminosity we carry out the radiation transport from heights $z/M = 50$ to $z/M = 200$ and assume the jet cross section (bounded by $\sigma \geqslant 0.1$) is emitting isotropically. The time-dependent SED is shown with a 2D color map where the y-axis indicates emission frequency and x-axis indicates increasing time in days, with the color indicating the specific luminosity. The frequency at peak synchrotron SED is $\nu_{\rm ssa} \sim 8 \times 10^{13}$ Hz, where $\nu_{\rm ssa}$ is the synchrotron self-absorption frequency and oscillates between $7.1 < \nu_{\rm ssa}/10^{13}\,{\rm Hz} < 9.3$. This $\nu_{\rm ssa}$ is also a "break" frequency below which, in the optically thick regime, there is no clear time variability. Above $\nu_{\rm ssa}$, in the optically thin regime, the SED shows clear time variability in the form of "fringes," indicating periodically increased specific luminosity. The eccentric binary spends more time in a "low" state, where the synchrotron emission specific luminosity is minimum, than in a "high state," where the specific luminosity has a sharp rise and decay in time. In Figure 5, we plot the synchrotron SED at the low (thick black line) and high (thin red line) states, selected at times $t = [44, 40]$ hr from the left panel of Figure 4. We indicate the synchrotron self-absorption frequency $\nu_{\rm ssa}$ with translucent vertical lines for each of the SEDs, and note that the peak frequency shifts by ∼30% between the low and high state occurring at $\nu_{\rm ssa} = [7.1,\ 9.3] \times 10^{13}$ Hz. Furthermore, the specific luminosity decreases from $L_\nu = 1.8$ to $1.0 \times 10^{23}\,{\rm erg\,s^{-1}\,Hz^{-1}}$ as the emission transitions from high to low. Our calculations predict that a smoking-gun synchrotron signature of more eccentric binaries is that they spend longer time in the low state than in the high state, and that the peak synchrotron frequency undergoes a shift between high and low states. This is consistent with eccentric binaries spending more time at apocenter than pericenter.

In the right panel of Figure 4, we show the Fourier transforms of the frequency-binned synchrotron SED. The y-axis is the frequency of the EM spectrum, and the x-axis is the frequency of the time variability (normalized by $f_{\rm orb}$) of the specific luminosity. The color map shows the strength of the PSD. The plot demonstrates that the synchrotron SED exhibits a periodicity on the orbital time $f \sim f_{\rm orb}$ for all EM frequencies in the optically thin regime (where $\nu_{\rm em} \gtrsim \nu_{\rm ssa}$) which is consistent with the dominant periodicity of its rest-mass accretion rate (Figure 2). This is the first explicit demonstration that an EM signature periodicity matches the accretion rate periodicity in BBH accretion.

We also experimented with different ways to set the energy density in the electron power-law distribution. If we do not assume a fixed ratio between the electron and magnetic energy density, then variability is not as clear. Moreover, when we adopt a thermal distribution for the electrons the variability in the synchrotron SED also becomes inconclusive, i.e., there is no clear dominant frequency in the periodogram. However, we emphasize that a full general-relativistic ray tracing and radiative transfer is necessary to determine the robustness of this finding.

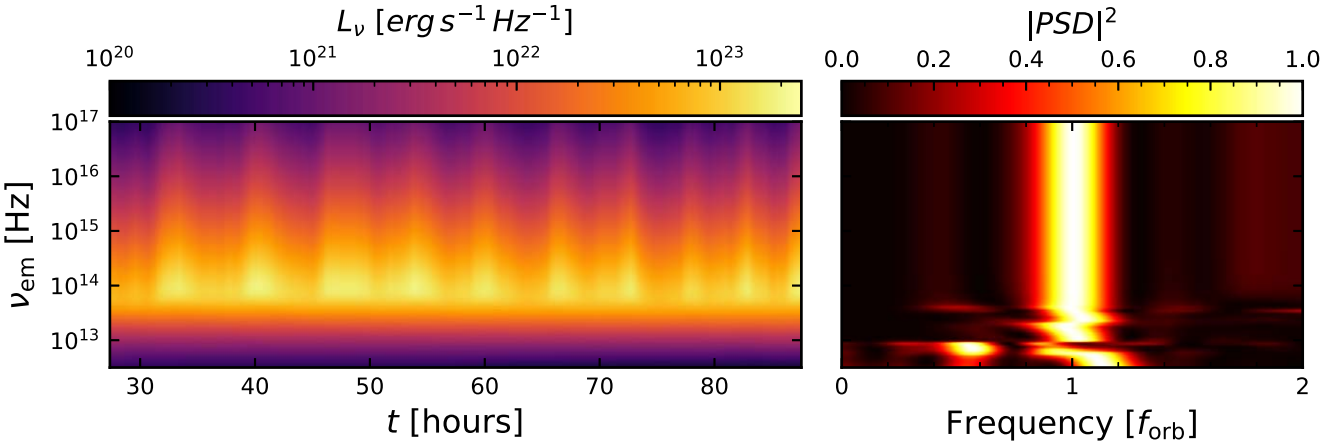

Figure 4. Left: specific luminosity of synchrotron emission on a color scale vs time for a $10^7\,M_\odot$ binary accreting at 10% Eddington. The y-axis is the frequency of the SED, and the x-axis is the time, with the color bar indicating the specific luminosity, L_ν. Right: PSD of the Fourier transform of the frequency-binned SED time series. We perform the Fourier transform for the time period $t > 4000\,M$ ($t > 54.7$ hr). The plots demonstrate that only the optically thin region $\nu_{em} \gtrsim 10^{14}$ Hz of the synchrotron SED has clear periodicity on the orbital timescale of $f \sim f_{orb}$, which matches its mass accretion rate periodicity and Poynting luminosity periodicity. There is no clear periodicity in the optically thick regime.

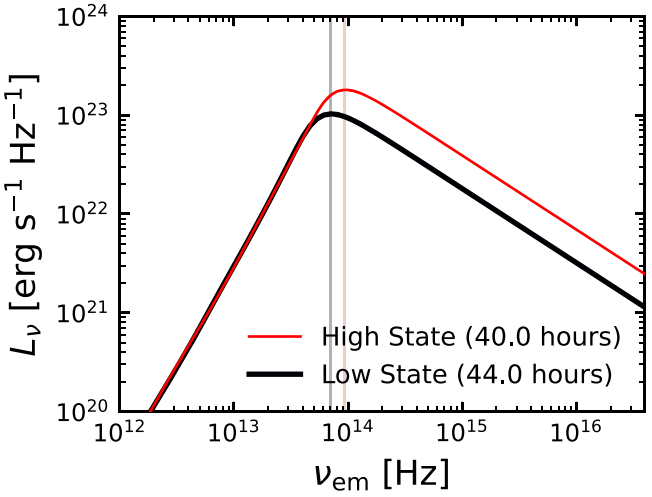

Figure 5. SED of the jet synchrotron emission at "low" (thick black line) and "high" (thin red line) states at $t = [44, 40]$ hr in Figure 4. The synchrotron self-absorption frequencies (vertical, translucent black and red lines) are $\nu_{ssa} = [7.1, 9.3] \times 10^{13}$ Hz, and the peak specific luminosities are $L_\nu = [1.0, 1.8] \times 10^{23}$ erg s^{-1} Hz^{-1} for the low and high states, respectively.

4.3. Coincident GW and EM Emission

In Figure 6, we showcase the coincident GW and EM emission from our SMBBH. We plot the amplitude of the $\ell = 2$, $m = 2$ mode of the GW strain (top panel), the outgoing Poynting luminosity normalized by the time-averaged rest-mass accretion rate (middle panel), and the optically thin synchrotron luminosity (bottom panel) integrated for frequencies $\nu_{em} \in [8 \times 10^{13}, 8 \times 10^{14}]$ Hz (which sample the SED near the peak) all vs retarded time. We indicate the GW peaks with vertical translucent lines in all three panels. The figure demonstrates that the GW and EM bursts happen almost simultaneously—the GW bursts marginally precede the EM bursts in certain cases (see the second, third, and fourth peaks). A smoking-gun multimessenger signature of binaries with nonnegligible eccentricity is that the time period between successive bursts is the same for both the GW and EM synchrotron emission.

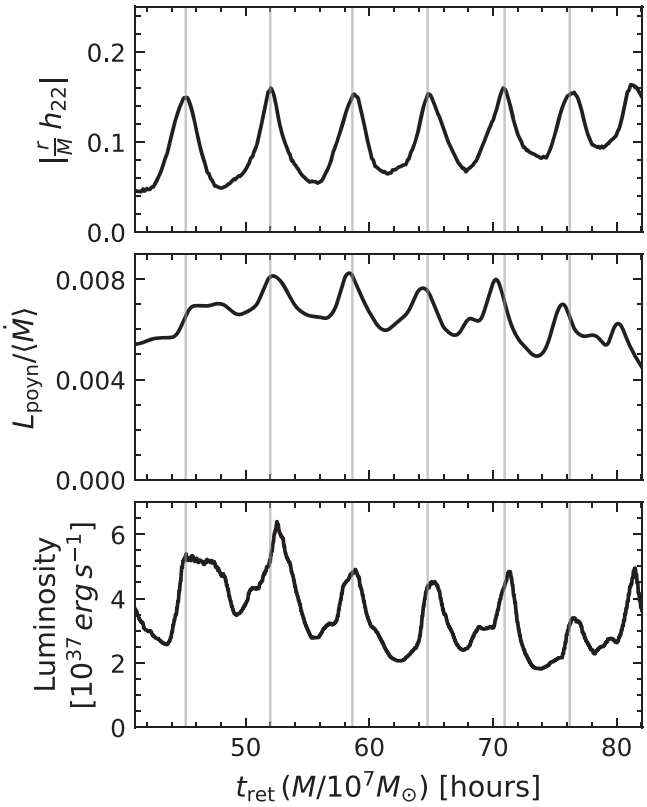

Figure 6. Top row: amplitude of the $\ell = 2$, $m = 2$ mode of the gravitational-wave (GW) strain, $|h_{22}|$, normalized by the distance r/M vs retarded time t_{ret}. Middle: outgoing Poynting luminosity normalized by the rest-mass accretion rate vs t_{ret}. Bottom: synchrotron luminosity integrated in the optically thin regime 8×10^{13} Hz $< \nu_{em} < 8 \times 10^{14}$ Hz vs. t_{ret}. We denote the location of GW bursts with vertical translucent gray lines on both the GW and EM panels. The lightcurves shows almost perfect alignment between GW, Poynting flux, and EM bursts.

4.4. Detectability of Synchrotron Emission

The synchrotron emission we report can be detected by NIRCam and MIRI on the James Webb Space Telescope (G. H. Rieke et al. 2015; T. P. Greene et al. 2017; G. S. Wright et al. 2023), the upcoming Rubin Observatory and the Legacy

Survey of Space and Time, as well as the Roman Space Telescope (Z. Ivezic et al. 2019). The sensitivity of these instruments places limits on the distance of the detectability of the synchrotron signatures we predict. We can solve for the maximum observable distance of our objects by starting with the equation for the AB magnitude of an object (J. B. Oke & J. E. Gunn 1983; M. S. Bessell 2005),

$$m = -2.5 \log_{10} \frac{F_\nu}{F_0}, \tag{1}$$

where m is the AB magnitude, F_ν is the specific flux of the object, and $F_0 = 3631\,\mathrm{Jy}$ is the reference flux, where $1\,\mathrm{Jy} = 10^{-23}\,\mathrm{erg\,s^{-1}\,cm^{-2}\,Hz^{-1}}$. The flux of our object can be expressed in terms of its specific luminosity,

$$F_\nu = L_\nu / 4\pi d^2, \tag{2}$$

where L_ν is the specific luminosity of our synchrotron radiation and d is the luminosity distance to the object. Solving for the distance ,we obtain

$$d = \sqrt{\frac{L_\nu}{4\pi F_0} 10^{m/2.5}}. \tag{3}$$

The most sensitive filter on NIRCam (F150W2) has a limiting magnitude of $m = 29.8$ for a 10^4 s exposure with a signal-to-noise ratio of 10 (T. P. Greene et al. 2017). Putting this into the equation, along with our calculated optically thin synchrotron specific luminosities, we can estimate the maximum distance our BBH could be observed out to. For example, we estimate that NIRCam could observe our $10^7\,M_\odot$ BBH with peak $L_\nu \sim 10^{23}\,\mathrm{erg\,s^{-1}\,Hz^{-1}}$ (see Figure 4) out to $\sim$0.2 Gpc, which corresponds to a redshift $z \sim 0.04$ assuming standard ΛCDM cosmology. We also repeated the calculation for a $10^9\,M_\odot$ BBH with peak $L_\nu \sim 10^{26}\,\mathrm{erg\,s^{-1}\,Hz^{-1}}$, which would be detectable out to $\sim$7 Gpc ($z \sim 1.1$) although, at these redshifts and binary mass, the optically thin synchrotron frequency would be redshifted into the F322W2 NIRCam filter, which has a lower limiting magnitude of $m = 29.1$, and MIRI filters, which, for its most sensitive filter (F560W), has a limiting magnitude of $m = 26.2$ (E. L. Wright 2006; T. P. Greene et al. 2017). Therefore, when evaluating more massive candidates at higher redshifts, a more careful calculation of the detectability is needed. All these distances are $\sim 5\times$ greater if we integrate for $z \geqslant 20\,M$ and the peak frequencies are blueshifted. Therefore, the above estimates are preliminary, and a more detailed radiative transfer calculation with ray tracing is necessary for more precise distances.

Additionally, we can roughly estimate the thermal emission of our CBD and minidisks. The inner parts of such accretion disks are radiation pressure dominated and optically thick due to Thompson scattering (S. L. Shapiro & S. A. Teukolsky 1983). Thompson scattering increases the path length of photons before they escape, which increases the photon's probability of absorption and reemission. This results in thermalization of the EM emission—we refer the reader to S. L. Shapiro & S. A. Teukolsky (1983) for a more detailed discussion. Therefore, using the fluid pressure, P, from our simulations, modeling it as $P = \frac{1}{3} a T^4$ (consistent with our choice of $\Gamma = 4/3$), and assuming that accretion takes place at 10% of the Eddington rate, we can solve for the temperature of the CBD and minidisk to estimate the ion temperature. We find this temperature to be $\mathcal{O}(10^6\,\mathrm{K})$. With corrections to the effective temperature and specific flux (Equations (14.5.54) and (14.5.51) from S. L. Shapiro & S. A. Teukolsky 1983, respectively) and integrating over the photosphere, we estimate the peak thermal emission frequency to be $\sim 10^{15}$ Hz with a peak specific flux of $F_{\mathrm{bb}} \sim 10^{24}\,\mathrm{erg\,s^{-1}\,Hz^{-1}}$. This is more luminous than our peak synchrotron emission at ν_{ssa} if our radiative transfer integration starts at $z/M = 50$. However, if we start our synchrotron radiation transfer at $z/M = 20$, the "high" states of our synchrotron time series become more luminous than the predicted blackbody emission from the entire disk and minidisks. Therefore, we tentatively predict the jet synchrotron emission to be observable over the disk thermal spectrum. We reiterate, however, that a more careful calculation of the jet, CBD, and minidisk emission with a full general-relativistic ray tracing and radiative transfer is necessary to more reliably decipher emission from these systems.

5. Conclusions

In this work, we presented the first simulation of MHD disk accretion onto an equal-mass, nonspinning, eccentric binary black hole in 3 + 1 full GR, incorporating synchrotron emission through the jet in postprocessing for the first time. Our key findings are the following:

1. The accretion rate onto eccentric BBHs in the strong-field dynamical spacetime regime has a periodicity that matches the binary orbital frequency $f \sim f_{\mathrm{orb}}$, unlike quasi-circular binaries for which this occurs at $f \sim 1.4\,f_{\mathrm{orb}}$.
2. Eccentric binaries exhibit periodicity in the Poynting luminosity and optically thin synchrotron emission at the orbital frequency, f_{orb}. A smoking-gun signature of eccentric binaries is that they spend more time in a low state (lower luminosity) than in a high state (higher luminosity), consistent with the time spent at apocenter and pericenter. Moreover, the peak synchrotron frequency shifts between the high and low states by $\sim$30%.
3. A smoking-gun multimessenger signature of eccentric binaries is quasiperiodic bursts in their GWs, optically thin synchrotron emission, and Poynting luminosity, with identical delay times for consecutive EM and GW bursts.

We also find that the synchrotron emission variability is sensitive to the choice of electron energy distribution—only a power-law electron distribution with a fixed ratio between electron and magnetic energy density demonstrates clear variability. Assuming no fixed ratio or a thermal electron distribution does not reveal a periodic synchrotron source. This could offer a unique opportunity to probe jet plasma physics with multimessenger observations with GWs: LISA BBHs that are found to have substantial eccentricity ($O(0.1)$) can be followed up with EM observations to test jet variability. The existence or not of variability of the synchrotron emission from the jet base in conjunction with theoretical modeling, such as that performed in this work, can allow us to understand how electrons adapt to the changing magnetic field in a BBH spacetime. For example, lack of variability at the binary orbital period would inform us that either the electrons near the jet base do not follow the magnetic field energy density or that they follow a thermal distribution. Regardless, the variability in the Poynting luminosity is robust, which implies that as the jet propagates into the interstellar and intergalactic medium, it

could generate emission in the radio that will exhibit variability on the binary orbital time.

We conclude by listing some caveats: a fully general-relativistic ray tracing and radiative transfer calculation is necessary to decipher the exact emission from the jet region down to the BH horizons and to understand EM emission from the CBD, the inner cavity, and the minidisks. The latter is expected to be responsible for the bulk of the X-ray/UV emission as well as Doppler-shifted emission lines (A. Sesana et al. 2012; T. Bogdanovic et al. 2022; M. Charisi et al. 2022). Radiation feedback becomes important for accretion rates near the Eddington regime and must be accounted for. As such, our results are most applicable to sub-Eddington SMBBHs. Finally, it is important to consider a wide range of disk initial data and include spinning BHs as well as other values of mass ratio and eccentricity. These will be the subject of future works of ours. However, the periodicities driven by eccentricity that we report should be robust. Hence, the qualitative features we have discovered in this work should be invariant under the aforementioned caveats as long as the eccentricity is high enough.

Acknowledgments

We thank Collin Christy for many useful discussions. This work was in part supported by NASA grant 80NSSC24K0771 and NSF grant PHY-2145421 to the University of Arizona. This research is part of the Frontera computing project at the Texas Advanced Computing Center. Frontera is made possible by U.S. National Science Foundation award OAC-1818253. This work used Stampede2 and Stamepede3 at the Texas Advanced Computing Center through allocation PHY190020 from the Advanced Cyberinfrastructure Coordination Ecosystem: Services & Support (ACCESS) program, which is supported by U.S. National Science Foundation grants 2138259, 2138286, 2138307, 2137603, and 2138296 (T. J. Boerner et al. 2023).

ORCID iDs

Vikram Manikantan https://orcid.org/0000-0003-0547-6158
Vasileios Paschalidis https://orcid.org/0000-0002-8099-9023
Gabriele Bozzola https://orcid.org/0000-0003-3696-6408

References

Abramowicz, M. A., Czerny, B., Lasota, J. P., & Szuszkiewicz, E. 1988, ApJ, 332, 646
Afzal, A., Agazie, G., Anumarlapudi, A., et al. 2023, ApJL, 951, L11
Aggarwal, K., Arzoumanian, Z., Baker, P. T., et al. 2019, ApJ, 880, 116
Alves, E., Zrake, J., & Fiuza, F. 2018, PhRvL, 121, 245101
Amaro-Seoane, P., Andrews, J., Arca Sedda, M., et al. 2023, LRR, 26, 2
Ansorg, M., Brügmann, B., & Tichy, W. 2004, PhRvD, 70, 064011
Arun, K. G., Belgacem, E., Benkel, R., et al. 2022, LRR, 25, 4
Avara, M. J., Krolik, J. H., Campanelli, M., et al. 2024, ApJ, 974, 242
Babak, S., Falxa, M., Franciolini, G., & Pieroni, M. 2024, PhRvD, 110, 063022
Baker, J., Haiman, Z., Rossi, E. M., et al. 2019, BAAS, 51, 123
Baker, J. G., Centrella, J., Choi, D.-I., Koppitz, M., & van Meter, J. 2006, PhRvL, 96, 111102
Balbus, S. A., & Hawley, J. F. 1991, ApJ, 376, 214
Barnes, J. E. 2002, MNRAS, 333, 481
Baumgarte, T. W., & Shapiro, S. L. 1998, PhRvD, 59, 024007
Bessell, M. S. 2005, ARA&A, 43, 293
Boerner, T. J., Deems, S., Furlani, T. R., Knuth, S. L., & Towns, J. 2023, in Practice and Experience in Advanced Research Computing 2023: Computing for the Common Good (New York: Association for Computing Machinery), 173
Bogdanovic, T., Miller, M. C., & Blecha, L. 2022, LRR, 25, 3
Bozzola, G. 2021, JOSS, 6, 3099
Bright, J. C., & Paschalidis, V. 2023, MNRAS, 520, 392
Campanelli, M., Lousto, C. O., Marronetti, P., & Zlochower, Y. 2006, PhRvL, 96, 111101
Cattorini, F., & Giacomazzo, B. 2024, APh, 154, 102892
Cattorini, F., Maggioni, S., Giacomazzo, B., et al. 2022, ApJL, 930, L1
Charisi, M., Bartos, I., Haiman, Z., Price-Whelan, A. M., & Márka, S. 2015, MNRAS, 454, L21
Charisi, M., Taylor, S. R., Runnoe, J., Bogdanovic, T., & Trump, J. R. 2022, MNRAS, 510, 5929
Chen, X., Madau, P., Sesana, A., & Liu, F. K. 2009, ApJL, 697, L149
Cheung, C. C., Harris, D. E., & Stawarz, L. 2007, ApJL, 663, L65
Chevalier, R. A. 1998, ApJ, 499, 810
Colella, P., & Woodward, P. R. 1984, JCoPh, 54, 174
Colpi, M., Holley-Bockelmann, K., Bogdanovic, T., et al. 2019, arXiv:1903.06867
DeLaurentiis, S., Haiman, Z., Westernacher-Schneider, J. R., et al. 2025, ApJ, 980, 55
Etienne, Z. B., Paschalidis, V., Haas, R., Moesta, P., & Shapiro, S. L. 2015, CQGra, 32, 175009
Etienne, Z. B., Paschalidis, V., Liu, Y. T., & Shapiro, S. L. 2012, PhRvD, 85, 024013
Farris, B. D., Gold, R., Paschalidis, V., Etienne, Z. B., & Shapiro, S. L. 2012, PhRvL, 109, 221102
Fedrigo, G., Cattorini, F., Giacomazzo, B., & Colpi, M. 2024, PhRvD, 109, 103024
Franchini, A., Prato, A., Longarini, C., & Sesana, A. 2024, A&A, 688, A174
Gold, R. 2019, Galax, 7, 63
Gold, R., Paschalidis, V., Etienne, Z. B., Shapiro, S. L., & Pfeiffer, H. P. 2014a, PhRvD, 89, 064060
Gold, R., Paschalidis, V., Ruiz, M., et al. 2014b, PhRvD, 90, 104030
Goodale, T., Allen, G., Lanfermann, G., et al. 2003, in Vector and Parallel Processing—VECPAR 2002, 5th Intnl. Conf., Lecture Notes in Computer Science (Berlin: Springer), 197
Graham, M. J., Djorgovski, S. G., Stern, D., et al. 2015, MNRAS, 453, 1562
Greene, T. P., Kelly, D. M., Stansberry, J., et al. 2017, JATIS, 3, 035001
Gutiérrez, E. M., Combi, L., Romero, G. E., & Campanelli, M. 2024, MNRAS, 532, 506
Ivezic, Z., Kahn, S. M., Tyson, J. A., et al. 2019, ApJ, 873, 111
Kelley, L. Z., Blecha, L., Hernquist, L., Sesana, A., & Taylor, S. R. 2018, MNRAS, 477, 964
Khan, A., Paschalidis, V., Ruiz, M., & Shapiro, S. L. 2018, PhRvD, 97, 044036
Kiehlmann, S., Vergara De La Parra, P., Sullivan, A., et al. 2024, arXiv:2407.09647
Kim, J. Y., Krichbaum, T. P., Lu, R. S., et al. 2018, A&A, 616, A188
Lai, D., & Muñoz, D. J. 2023, ARA&A, 61, 517
Li, S., Berczik, P., Chen, X., et al. 2019, ApJ, 883, 132
Liu, T., Gezari, S., Ayers, M., et al. 2019, ApJ, 884, 36
Manikantan, V., Paschalidis, V., & Bozzola, G. 2025, arXiv:2504.12375
Medina-Torrejón, T. E., de Gouveia Dal Pino, E. M., Kadowaki, L. H. S., et al. 2021, ApJ, 908, 193
Most, E. R., & Wang, H.-Y. 2024, ApJL, 973, L19
Most, E. R., & Wang, H.-Y. 2025, PhRvD, 111, L081304
Muñoz, D. J., Lai, D., Kratter, K., & Miranda, R. 2020, ApJ, 889, 114
Ni, Y., Di Matteo, T., Chen, N., Croft, R., & Bird, S. 2022, ApJL, 940, L49
Oke, J. B., & Gunn, J. E. 1983, ApJ, 266, 713
O'Neill, S., Kiehlmann, S., Readhead, A. C. S., et al. 2022, ApJL, 926, L35
Panaitescu, A., & Kumar, P. 2002, ApJ, 571, 779
Paschalidis, V., Bright, J., Ruiz, M., & Gold, R. 2021, ApJL, 910, L26
Paschalidis, V., Etienne, Z. B., Gold, R., & Shapiro, S. L. 2013, arXiv:1304.0457
Peters, P. C., & Mathews, J. 1963, PhRv, 131, 435
Petropoulou, M., Sironi, L., Spitkovsky, A., & Giannios, D. 2019, ApJ, 880, 37
Porter, K., Noble, S. C., Gutiérrez, E. M., et al. 2025, ApJ, 979, 155
Porth, O., Chatterjee, K., Narayan, R., et al. 2019, ApJS, 243, 26
Rieke, G. H., Wright, G. S., Böker, T., et al. 2015, PASP, 127, 584
Rodriguez, C., Taylor, G. B., Zavala, R. T., et al. 2006, ApJ, 646, 49
Rodriguez, C., Taylor, G. B., Zavala, R. T., Pihlström, Y. M., & Peck, A. B. 2009, ApJ, 697, 37
Roedig, C., Dotti, M., Sesana, A., Cuadra, J., & Colpi, M. 2011, MNRAS, 415, 3033
Rosado, P. A., Sesana, A., & Gair, J. 2015, MNRAS, 451, 2417

Ruiz, M., Tsokaros, A., & Shapiro, S. L. 2023, PhRvD, 108, 124043
Rybicki, G., & Lightman, A. 1991, Radiative Processes in Astrophysics (New York, NY: Wiley)
Ryu, T., Perna, R., Haiman, Z., Ostriker, J. P., & Stone, N. C. 2018, MNRAS, 473, 3410
Saikia, D. J. 2022, JApA, 43, 97
Schnetter, E., Hawley, S., & Hawke, I., 2016 Carpet: Adaptive Mesh Refinement for the Cactus Framework, Astrophysics Source Code Library, ascl:1611.016
Schnittman, J. D. 2011, CQGra, 28, 094021
Scott, M. A., & Readhead, A. C. S. 1977, MNRAS, 180, 539
Sesana, A., Roedig, C., Reynolds, M. T., & Dotti, M. 2012, MNRAS, 420, 860
Shapiro, S. L., & Teukolsky, S. A. 1983, Black Holes, White Dwarfs and Neutron Stars. The Physics of Compact Objects (New York, NY: Wiley)
Shibata, M., & Nakamura, T. 1995, PhRvD, 52, 5428
Siwek, M., Kelley, L. Z., & Hernquist, L. 2024, MNRAS, 534, 2609
Sperhake, U. 2007, PhRvD, 76, 104015
Thornburg, J. 2004, CQGra, 21, 743
Thorpe, J. I., Ziemer, J., Thorpe, I., et al. 2019, BAAS, 51, 77
Toro, E. F. 2009, Riemann Solvers and Numerical Methods for Fluid Dynamics: A Practical Introduction (Berlin: Springer)
Tsouros, A., & Kylafis, N. D. 2017, A&A, 603, L4
Valli, R., Tiede, C., Vigna-Gómez, A., et al. 2024, A&A, 688, A128
Virtanen, P., Gommers, R., Oliphant, T. E., et al. 2020, NatMe, 17, 261
Walker, R. C., Hardee, P. E., Davies, F. B., Ly, C., & Junor, W. 2018, ApJ, 855, 128
Werneck, L., Cupp, S., Assumpção, T., et al. 2023, The Einstein Toolkit, Zenodo, doi:10.5281/zenodo.7942541
Westernacher-Schneider, J. R., Zrake, J., MacFadyen, A., & Haiman, Z. 2022, PhRvD, 106, 103010
Witek, H., & Zilhão, M., 2015 Canuda, bitbucket, https://bitbucket.org/canuda/
Witek, H., Zilhao, M., Bozzola, G., et al. 2021, Canuda: A Public Numerical Relativity Library to Probe Fundamental Physics v2, Zenodo, doi:10.5281/zenodo.5520862
Wright, E. L. 2006, PASP, 118, 1711
Wright, G. S., Rieke, G. H., Glasse, A., et al. 2023, PASP, 135, 048003
Yadav, J., Das, M., Barway, S., & Combes, F. 2021, A&A, 651, L9